

# 3D massless Kane fermions observed in a zinc-blende crystal

M. Orlita,<sup>1,2,\*</sup> D. M. Basko,<sup>3</sup> M. S. Zholudev,<sup>4,5</sup> F. Teppe,<sup>4</sup> W. Knap,<sup>4</sup> V. I. Gavrilenko,<sup>5</sup> N. N. Mikhailov,<sup>6</sup> S. A. Dvoretiskii,<sup>6</sup> P. Neugebauer,<sup>7</sup> C. Faugeras,<sup>1</sup> A.-L. Barra,<sup>1</sup> G. Martinez,<sup>1</sup> and M. Potemski<sup>1</sup>

<sup>1</sup>Laboratoire National des Champs Magnétiques Intenses, CNRS-UJF-UPS-INSA, Grenoble, France

<sup>2</sup>Charles University, Faculty of Mathematics and Physics, Ke Karlovu 5, 121 16 Praha 2, Czech Republic

<sup>3</sup>Université Grenoble 1/CNRS, LPMMC UMR 5493, B.P. 166, 38042 Grenoble, France

<sup>4</sup>Laboratoire Charles Coulomb (L2C), UMR CNRS 5221,

GIS-TERALAB, Université Montpellier II, 34095 Montpellier, France

<sup>5</sup>Institute for Physics of Microstructures, RAS, Nizhny Novgorod, Russia

<sup>6</sup>A.V. Rzhanov Institute of Semiconductor Physics, Siberian Branch, Russian Academy of Sciences, Novosibirsk 630090, Russia

<sup>7</sup>Institut für Physikalische Chemie, Universität Stuttgart, Pfaffenwaldring 55, 70569 Stuttgart, Germany

Solid state physics and quantum electrodynamics with its ultra-relativistic (massless) particles meet, to their mutual benefit, in the electronic properties of one-dimensional carbon nanotubes as well as two-dimensional graphene or surfaces of topological insulators. However, clear experimental evidence for electronic states with conical dispersion relations in all three dimensions, conceivable in certain bulk materials, is still missing. In the present work, we fabricate and study a zinc-blend crystal, HgCdTe, at the point of the semiconductor-to-semimetal topological transition. Three-dimensional massless electrons with a velocity of about  $10^6$  m/s are observed in this material, as testified by: (i) the dynamical conductivity which increases linearly with the photon frequency, (ii) in a magnetic field  $B$ , by a  $\sqrt{B}$  dependence of dipole-active inter-Landau-level resonances and (iii) the spin splitting of Landau levels, which follows a  $\sqrt{B}$  dependence, typical of ultra-relativistic particles but not really seen in any other electronic system so far.

The physics of “Dirac cones”, which largely dominates the research on electronic properties of 1D and 2D allotropes of  $sp^2$ -bonded carbon<sup>1–3</sup> as well as topological insulators<sup>4,5</sup>, is now anticipated to be also explored in 3D solids. Indeed, there have recently been a number of theoretical predictions of a class of fairly novel materials with conical 3D electronic bands, such as Weyl semimetals (with even number of momentum points where two conical bands touch) and Dirac semimetals (with one or more momentum points, in which four conical bands meet). Those compounds, such as the metastable  $\beta$ -cristobalite BiO<sub>2</sub> (Ref. 6), pyrochlore iridates such as Y<sub>2</sub>Ir<sub>2</sub>O<sub>7</sub> (Ref. 7 and 8), A<sub>3</sub>Bi where A is an alkali metal Na, K, or Rb (Ref. 9), distorted spinels (Ref. 10), as well as TlBi(S<sub>1–x</sub>Te<sub>x</sub>)<sub>2</sub> and TlBi(S<sub>1–x</sub>Se<sub>x</sub>)<sub>2</sub> (Ref. 11), will be possibly probed experimentally in the future, to clarify their bulk electronic structure. The surface states of the latter compound have already been probed experimentally<sup>12,13</sup>.

On the other hand, the presence of 3D conical dispersion relations of electronic states was suggested a long time ago<sup>14</sup> to be possible in more conventional, zinc-blende compounds known as narrow-gap semiconductors. On experimental ground, this particular shape of dispersion relations has not been seen as the main focus of studies so far. Nevertheless, a number of investigations, particularly intense in the sixties and seventies and including magneto-optical studies,<sup>15–19</sup> have shown that the effective mass of the carriers and the energy band gap in Hg<sub>1–x</sub>Cd<sub>x</sub>Te (MCT) can be made very small. The band gap was estimated down to tens of meV and the

effective mass to  $10^{-2}$  in samples with cadmium concentration close to  $x = 0.17$ . This could be a sign of linear dispersion relations, though previous experiments studies might have suffered the insufficient sample quality (inhomogeneous chemical composition and high, unintentional doping) to be more conclusive.

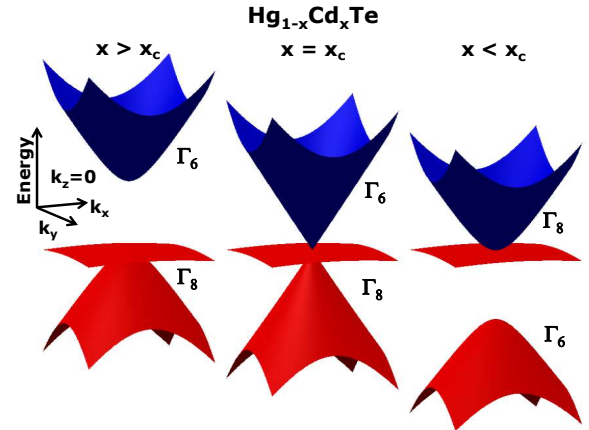


FIG. 1. A schematic view of the electronic dispersion of MCT at  $k_z = 0$  for three different cadmium concentrations  $x$ . A standard gapped semiconductor for  $x > x_c$  becomes a semimetal at  $x < x_c$ . At the point of the topological transition,  $x = x_c$ , the conduction band and the light-hole valence band have a 3D conical dispersion, which is crossed at the vertex by an almost flat heavy-hole band. In all parts, blue color corresponds to the conduction band, the valence bands are depicted in red.

If the cadmium content is sufficiently high,  $x > x_c \approx 0.17$ , the MCT compounds are conventional (narrow gap) semiconductors with the standard sequence of different symmetry bands: the  $s$ -type  $\Gamma_6$  band is fixed above the  $p$ -type  $\Gamma_8$  bands, as schematically shown in Fig. 1. Instead, if  $x < x_c$ , the band order is inverted: the  $\Gamma_6$  band lies below the  $\Gamma_8$  bands. As the two  $\Gamma_8$  bands always touch each other at the  $\Gamma$  point of the first Brillouin zone, and only the lower band is occupied in the intrinsic case, for  $x < x_c$  the band structure is gapless, and MCT becomes a semimetal. The two distinct phases are not topologically equivalent, as characterized by a  $Z_2$  topological invariant<sup>20</sup>. At the point of the topological transition, when the cadmium concentration reaches its critical value,  $x = x_c$ , the bandgap shrinks to zero<sup>19</sup> and the electronic dispersion relation presents some very peculiar properties.

These conical bands have several spectacular properties similar to those in Dirac and Weyl semimetals (such as Klein tunnelling and suppressed backscattering, as discussed below). Nevertheless, a crucial difference must be stressed. Weyl semimetals are topologically protected, i.e., the Weyl points are stable with respect to small per-

turbations. Dirac semimetals are not topologically protected, but can be protected by the crystal symmetry (i.e., the Dirac points are stable with respect to perturbations which preserve this symmetry). The conical dispersion in the gapless MCT is not protected by symmetry or topology; rather, it is achieved by fine tuning of a system parameter (cadmium concentration). The protected bands might be robust and then advantageously unaffected by small changes of external parameters. On the other hand, the band structure of MCT can be suitably engineered in benefit to design and fabricate the “gapped-at-will” compounds and their interfaces with massless systems.

The basic theoretical approach, needed to understand these properties, is based on the standard Kane model<sup>21</sup>, whose validity for MCT has been confirmed by a number of previous studies<sup>15–18</sup> and which usually implies more than 10 free parameters.<sup>19</sup> Here, we retain only the terms linear in the wave vector, and neglect the split-off  $\Gamma_7$  band [the magnitude of the splitting,  $\Delta \approx 1$  eV (Refs. 19 and 22) is assumed to be sufficiently large]. For the remaining six bands, the Hamiltonian can be written as (see Supplementary Information):

$$H(\mathbf{k}) = \begin{pmatrix} 0 & vk_+\sqrt{3}/2 & -vk_-/2 & 0 & 0 & -vk_z \\ vk_-\sqrt{3}/2 & 0 & 0 & 0 & 0 & 0 \\ -vk_+/2 & 0 & 0 & -vk_z & 0 & 0 \\ 0 & 0 & -vk_z & 0 & -vk_-\sqrt{3}/2 & vk_+/2 \\ 0 & 0 & 0 & -vk_+\sqrt{3}/2 & 0 & 0 \\ -vk_z & 0 & 0 & vk_-/2 & 0 & 0 \end{pmatrix} \equiv v\mathbf{k} \cdot \mathbf{J}, \quad (1)$$

where  $k_{\pm} = k_x \pm ik_y$ , and the velocity  $v = \sqrt{E_P/(3m_0)} \approx 10^6$  m/s is expressed in terms of the free electron mass  $m_0$  and the Kane energy  $E_P$  (typically,  $E_P \approx 20$  eV for zinc blende semiconductors, see, e.g., Ref. 23). The velocity is thus the only free parameter, which makes this model extremely simple.

The Hamiltonian (1) has three eigenvalues, each doubly degenerate due to the Kramers theorem (time-reversal symmetry):

$$E_{\mathbf{k}} = 0, \pm v|\mathbf{k}| \quad (2)$$

As usual, the two components of the Kramers doublet can be labelled by two spin projections  $\downarrow, \uparrow$ , even though this degree of freedom has a strong admixture of the orbital motion due to the spin-orbit coupling. This implies an anomalously large and nonlinear Zeeman effect.

The eigenvalue  $E_{\mathbf{k}} = 0$  corresponds to the heavy-hole band which, in the approximation of Eq. (1), is dispersionless (completely flat) or, in other words, characterized by an infinite effective mass. The inclusion of parabolic terms in the electron dispersion results in a downward bending of the heavy-hole band, away from  $\mathbf{k} = 0$ . This curvature, corresponding to a heavy-hole

mass of about  $m_{hh} \approx 0.5 m_0$ <sup>19</sup>, is not sensitive to the topological transition at  $x = x_c$ . The simplified picture of massless and infinite-mass particles can be used at sufficiently low energies  $E$ , such that the “relativistic” mass of massless fermions,  $m_c = E/v^2 \ll m_{hh}$ . This defines the energy cutoff of  $m_{hh}v^2 \approx 3$  eV, less stringent than the spin-orbit splitting  $\Delta \approx 1$  eV. One step beyond the approximation of Eq. (1) is therefore to use the eight-band model with a finite  $\Delta$  though still ignoring the apparent dispersion of the heavy hole band (see Supplementary Information for details). We follow such an approach when it is necessary to refine the analysis of the experimental data.

The matrices  $\mathbf{J} = \{J_x, J_y, J_z\}$  which appear in Eq. (1) do not satisfy the algebra of angular momentum 1, nor any other closed algebra. Notably, the massless fermions in MCT are not equivalent to the three-dimensional Dirac electrons in the ultra-relativistic limit of the quantum electrodynamics (QED). For example, the Hamiltonian in Eq. (1) has the characteristic property:

$$U_c H(\mathbf{k}) U_c = -H(\mathbf{k}), \quad U_c \equiv \text{diag}(1, -1, -1, 1, -1, -1). \quad (3)$$

Note, however, that there are more  $-1$ 's than  $1$ 's in  $U_c$ , hence it is not the usual chiral property. As discussed in the Supplementary Information, the property (3) ensures the existence of a doubly-degenerate flat band. To the best of our knowledge, the Hamiltonian (1) does not reduce to any well-known case of massless particles in quantum electrodynamics. We therefore invoke a new term ‘‘Kane fermions’’ to refer to the electronic states of MCT at the point of the topological transition (to states in gapless MCT).

Massless Kane fermions share, however, a number of properties with other ultrarelativistic particles. A prominent example is Klein tunnelling invoked for 3D Dirac electrons in QED and apparent for 2D Dirac electrons in graphene<sup>25,26</sup>. A perfect transmission through an arbitrarily high potential barrier at normal incidence, due to the Klein paradox, should also occur in a gapless MCT. This can be seen by noting that the eigenstates corresponding to the same (e. g., positive) energy but to opposite wave vectors  $\mathbf{k}$ ,  $-\mathbf{k}$ , also correspond to different eigenvalues,  $\pm 1$ , of the projection of  $\mathbf{J}$  on  $\mathbf{k}$ . Thus, a potential which does not change  $\mathbf{J}$  (such as the electrostatic potential which acts in the same way on electrons in all bands and thus is proportional to the unit matrix), cannot backscatter an electron in the conduction band.

In order to prove the concept of massless Kane fermions in experiments, we have used the MBE technique to grow thin layers of MCT on semi-insulating GaAs substrates (see Supplementary Information). The optimal structure was used for measurements. It contains an MCT layer with cadmium concentration close to  $x_{\text{Cd}} = 0.17$  which extends over a thickness of  $d \approx 3.2 \mu\text{m}$ . The relevant part of this MCT layer is sufficiently thick to be considered a 3D material and at the same time thin enough to be suitable for our optical transmission experiments.

A striking consequence of conical dispersions on the optical properties of 3D massless fermions is the absorption coefficient  $\lambda(\omega)$  being proportional to the frequency  $\omega$ , distinctly in contrast to frequency independent absorption of 2D Dirac electrons as observed in graphene<sup>27,28</sup>. In simple words, these characteristic dependences result from the particular forms of the joint density of states  $\mathcal{D}(\omega)$ , which define the basic absorption profile in solids:  $\lambda(\omega) \propto \mathcal{D}(\omega)/\omega$ . A conical dispersion in 2D yields  $\mathcal{D}(\omega) \propto \omega$ , whereas it implies  $\mathcal{D}(\omega) \propto \omega^2$ , and thus  $\lambda(\omega) \propto \omega$  in case of a 3D system with massless particles.

To be more quantitative, we use a simple form of the Hamiltonian given by Eq. (1) and follow the standard recipe<sup>23</sup> to analytically derive the dielectric function  $\varepsilon(\omega)$  of the system (see Supplementary Information). Fixing  $\Omega$  for the high-energy cut-off of the conical dispersion, one finds that if  $\omega \ll \Omega$ , then:<sup>24</sup>

$$\varepsilon(\omega) = \varepsilon_\infty + \alpha \frac{13}{12} \frac{c}{v} \left( \frac{2}{\pi} \ln \frac{\Omega}{|\omega|} + i \text{sign} \omega \right), \quad (4)$$

where  $\alpha$  is the fine structure constant ( $\alpha \approx 1/137$ )

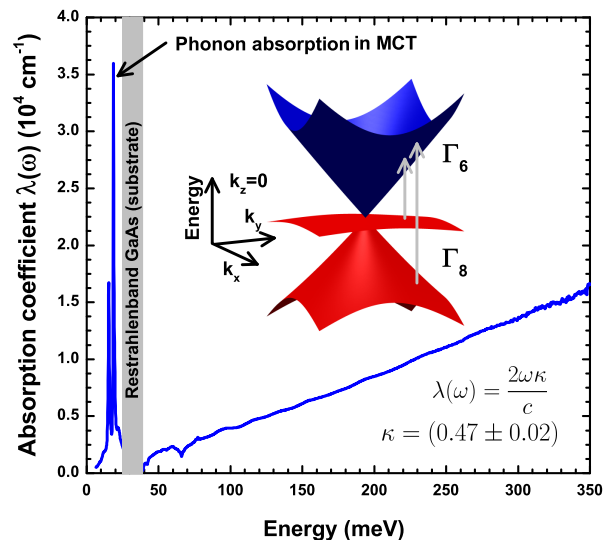


FIG. 2. Absorption coefficient of MCT at zero magnetic field,  $\lambda_{B=0}$ , measured experimentally, see the text and Methods for details. While the low-energy response is dominated by absorption due to phonons, the linear dependence on  $\omega$  at higher photon energies is directly linked to the conical dispersion of 3D massless fermions. The interband absorption in gapless MCT, schematically shown in the inset, is dominated by transitions from the flat (heavy-hole) band.

and  $\varepsilon_\infty$  accounts for the contribution from transitions other than those described by Eq. (1). The dissipative part of the dielectric function,  $\text{Im} \varepsilon(\omega)$ , is dispersionless, while  $\text{Re} \varepsilon(\omega)$  gains a weak (logarithmic) dependence on  $\omega$ . Consequently, we derive the dynamical conductivity,  $\sigma(\omega) = i(1 - \varepsilon)\varepsilon_0\omega$ , the real part of which is a linear function of  $\omega$ . Let us note that (interband) absorption in gapless MCT is dominated by transitions from the flat (heavy-hole) band, which is fully occupied in the intrinsic (undoped) material.

Equation (4) implies a nearly frequency-independent extinction coefficient  $\kappa = \text{Im} \sqrt{\varepsilon(\omega)}$ , and consequently, the absorption coefficient  $\lambda(\omega)$  increasing linearly with  $\omega$ ,  $\lambda(\omega) = 2\kappa\omega/c$ . The experimentally observed value  $\kappa = 0.47 \pm 0.02$  derived directly from the data shown in Fig. 2 agrees fairly well with the extinction coefficient,  $\kappa \approx 0.4$ , calculated using Eq. 4, see Methods for more details.

In a strong magnetic field, the 3D dispersion is transformed into a set of Landau levels (LLs), or more precisely, into 1D Landau bands which disperse with the momentum component along the field ( $z$  axis). Inserting the magnetic field into the Hamiltonian in Eq. (1) via the standard Peierls substitution,  $\hbar\mathbf{k} \rightarrow \hbar\mathbf{k} - e\mathbf{A}$ , one obtains for gapless MCT the LL energies [see Eq. (S28) of the Supplementary Information]:

$$E_{\zeta,n,\sigma}(k_z) = \zeta \hbar v \sqrt{(2n - 1 + \sigma/2)l_B^{-2} + k_z^2}, \quad (5)$$

where  $l_B^{-2} = eB/\hbar$  and the LL index  $n = 0, 1, 2, \dots$ . For

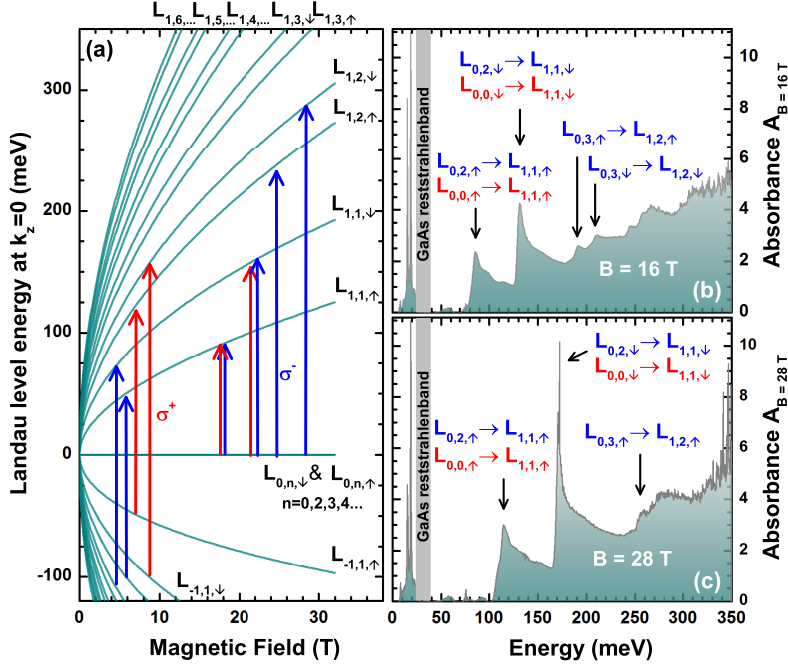


FIG. 3. Part (a): Landau levels (for  $k_z = 0$ ) in gapless MCT,  $L_{\zeta,n,\sigma}$ , as a function of the magnetic field, calculated using the eight-band model, using only  $v$  and  $\Delta$  parameters. Arrows of different colors show the optically allowed transitions in undoped gapless MCT in the two circular polarizations  $\sigma^+$  and  $\sigma^-$ . Parts (b) and (c): Experimentally measured absorption coefficient  $\lambda_B$  (absorbance) as a function of the photon energy, presented for two values of the magnetic field,  $B = 16$  and  $28$  T, respectively.

$n \geq 2$ , the band index is  $\zeta = 1, 0, -1$ , while at  $n = 1$  only  $\zeta = \pm 1$  are allowed and at  $n = 0$  only  $\zeta = 0$  exists. The states in the flat band remain at zero energy, because the property (3) remains valid in the presence of a magnetic field.

The quantum number  $\sigma = \pm 1$  shows how the Kramers degeneracy, mentioned above, is lifted by the magnetic field. Thus,  $\sigma$  can be viewed as the spin projection on the magnetic field. The spin splitting is entirely determined by the orbital parameters  $v$ ,  $n$ , and  $k_z$ . Moreover, at  $k_z = 0$  the spin splitting of all Landau levels is proportional to  $\sqrt{B}$ , which means that the  $g$  factor defined in the standard way,  $g_{\zeta,n} = (E_{\zeta,n,\uparrow} - E_{\zeta,n,\downarrow})/(\mu_B B)$ , diverges at  $B \rightarrow 0$ . This is quite unusual for a solid state system, and, in particular, does not hold for the Dirac fermions in graphene. On the other hand, such behavior is characteristic of ultrarelativistic Dirac electrons in QED,  $E_{\zeta,n,\sigma}(k_z) = \zeta \hbar c \sqrt{(2n+1+\sigma)/l_B^2 + k_z^2}$ , where  $n = 0, 1 \dots$  and  $\zeta = \pm 1$ , see, e.g., Ref. 30. Note, however, an essential difference: in QED, a level  $(n, \sigma = +1)$  is degenerate with the level  $(n+1, \sigma = -1)$ . Such degeneracy is absent for Kane fermions, since it is  $\sigma/2$  that enters Eq. (5). The  $\sqrt{B}$  spin splitting occurs in MCT because the strength of the spin-orbit coupling becomes effectively infinite when the energy gap vanishes. Let us now discuss how the  $\sqrt{B}$  dependence of LLs and also of the spin splitting at  $k_z = 0$ , described by Eq. (5), is verified experimentally.

The magneto-optical response of MCT is determined by electric-dipole selection rules:  $\Delta n = n \pm 1$  with “ $\pm$ ” corresponding to the two circular polarizations,  $\Delta k_z = 0$ ,  $\Delta \sigma = 0$ , and no restriction on  $\zeta$ . In the undoped MCT, the incident photon can excite electrons from the filled valence bands,  $\zeta = -1, 0$ , to the empty conduction band,

$\zeta = 1$ , as shown schematically in Fig. 3(a). Examples of the measured spectra are shown in Fig. 3(b). Since the dispersion of each Landau band near  $k_z = 0$  is parabolic, the joint density of states has sharp inverse-square-root singularities at energies of the transitions with  $k_z = 0$ , with an abrupt cutoff on the low-energy side and a shoulder on the high-energy side, as expected also for Weyl semimetals.<sup>31</sup> In the absence of a magnetic field, such a density of states can be found in 1D Dirac-type systems, in particular, in carbon nanotubes<sup>1</sup>. Note that the singularity of the lowest transition is less sharp than that of the next one. We attribute this to a small residual electronic doping, which results in filling of the states with very small  $k_z$  in the lowest Landau level in the conduction band ( $L_{1,1,\uparrow}$ ), so that the optical transition involving these states is blocked by the Pauli principle, thereby cutting off the singularity.

The key feature of the massless fermions, expressed by Eq. (5) is the  $\sqrt{B}$ -dependence of the transition energies at  $k_z = 0$ . In Fig. 4, we plot the infrared absorbance spectrum (relative to the zero-field absorbance) for magnetic fields up to 31 T. When plotted as a function of  $\sqrt{B}$ , the positions of the  $k_z = 0$  singularities guide the eye along straight lines. A close inspection shows that they are slightly curved at high fields. This weak curvature can be accounted for by including the spin-orbit split-off band with  $\Delta = 1$  eV. The theoretical curves in Fig. 4 were produced using such an 8-band model, considering  $v_F$  and  $\Delta$  as only two parameters. The two brightest lines correspond to the transitions from the flat band to the two spin-split components of the first Landau level in the conduction band (levels  $L_{1,1,\uparrow}$  and  $L_{1,1,\downarrow}$ , see Fig. 3(a)). This agreement between experiment and theory provides us with another fingerprint of 3D massless fermions in

gapless MCT. Let us note the  $\sqrt{B}$ -dependence does not serve as a unique signature of 3D massless particles and it can be found, for a certain range of magnetic fields, in the optical response of other bulk materials, e.g., in highly anisotropic graphite and bismuth<sup>32,33</sup>.

Having shown that in a wide, 30 – 300 meV energy range, the optical response of our sample is well explained by a model of gapless and intrinsic (undoped) MCT, we focus now on the low energy, low magnetic field range (see Fig. 5) of our data, with the aim of estimating the accuracy of such an approach. The spectral range of interest, below 30 meV, is not easy to explore because of strong phonon contributions to the absorption, which mask the evolution of electronic resonances. Nevertheless, a slight deviation of the experimental data from a model of an ideal, gapless and intrinsic MCT becomes apparent.

Firstly, we concentrate on two, most pronounced interband transitions in the region around 25 meV and conclude that they appear at higher energies than those expected from simple calculations using Eq. (5). This discrepancy points towards an MCT with a small but still non-zero gap  $E_g$ . Setting  $E_g = 4$  meV in calculations we satisfactorily improve the data modelling (see solid lines in Fig. 5).

The second relevant observation is that the interband transitions, which are strong at higher energies, rather suddenly weaken in the limit of low magnetic fields. At the same time the lowest energy interband transition transforms into a resonance which follows a linear rather than  $\sqrt{B}$  dependence in small magnetic fields. These

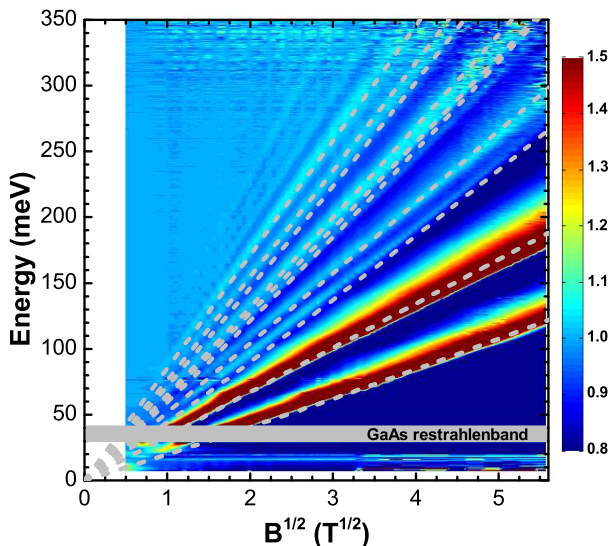


FIG. 4. Relative change of absorbance  $A_B/A_{B=0}$  plotted as a false color-map. All the observed resonances clearly follow  $\sqrt{B}$ -dependence. The dashed lines are calculated positions of inter-LL resonances at  $k_z = 0$  using parameters  $v_F = 1.06 \times 10^6$  m/s and  $\Delta = 1$  eV. The presence of the spin-orbit split band, expressed by parameter  $\Delta$ , does not qualitatively change the LL spectrum, but introduces a weak electron-hole asymmetry.

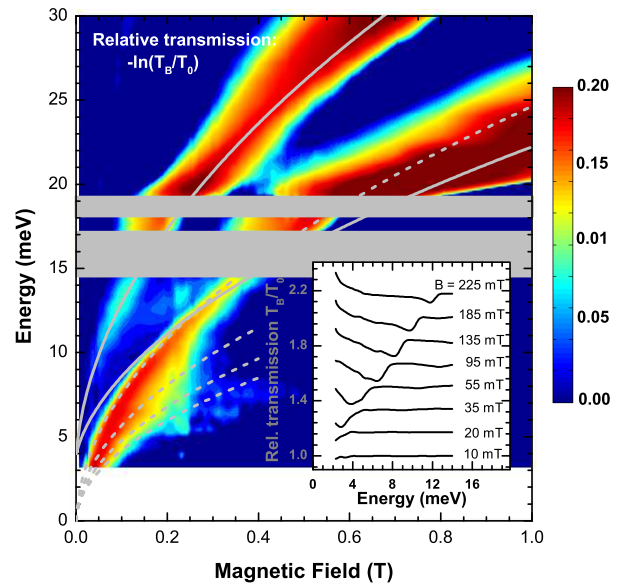


FIG. 5. Relative change of transmission, plotted as  $-\ln[T_B/T_0]$ , in a form of a color-map at low fields. The inset shows selected transmission spectra, in which the well-defined CR response is observed down to 30 mT. The solid and dashed lines correspond to expected positions of inter-LL transition in a MCT system with  $v = 1.06 \times 10^6$  m/s and small energy gap of  $E_g = 4$  meV. Solid lines show two lowest lying interband resonances (from the flat band to  $L_{1,1,\uparrow}$  and  $L_{1,1,\downarrow}$  levels), the dashed lines are pure CR-like transitions between pairs of adjacent LLs in the conduction band ( $\zeta = 1, n = 1, 2, 3 \dots$ ). The grey areas correspond to regions of strong phonon-related absorption in MCT.

effects indicate that our structure is not perfectly intrinsic but characterized by a nonzero electron concentration (Fermi energy  $E_F$  in the conduction band). Indeed, if the electron concentration is not zero, each interband Landau level transition must be (Pauli) blocked at sufficiently low fields, when the corresponding electronic Landau level crosses below the Fermi energy. Our interband transitions are barely seen at energies below 15 meV, see Fig. 5. This allows us to estimate  $E_F \approx 15 - 17$  meV, and in consequence also the electron concentration  $n = \frac{1}{3\pi^2 v^3 \hbar^3} [E_F(E_F - E_g)]^{3/2} = (2 - 3) \times 10^{14}$  cm<sup>-3</sup> (for  $E_g = 4$  meV estimated above).

The presence of free electrons in our structure explains also its spectral response at low energies (below 15 meV). This response is due to classical cyclotron resonance absorption at low magnetic fields, which transforms with increasing  $B$  into intraband transitions between adjacent Landau levels and ends up as a transitions from the flat band into  $L_{1,1,\uparrow}$  level, see Fig. 3(a), when  $E_F$  is locked at the bottom of  $L_{1,1,\uparrow}$  level. It is worth noticing that, independently of parabolic or linear electronic dispersions, the classical cyclotron resonance is linear with the magnetic field, invoking a  $m_c = E_F/v^2$  effective mass in case of linear dispersion relations<sup>34-36</sup>. In our case, a small gap is present and the cyclotron mass becomes  $m_c =$

$(E_F - E_g/2)/v^2 \approx 2 \times 10^{-3} m_0$ . This value corresponds well to the cyclotron mass,  $m_c = (1.5 \pm 0.5) \times 10^{-3} m_0$  derived directly from the slope of cyclotron resonance absorption in the limit of low magnetic fields.

In conclusion, we have observed a new type of 3D massless fermions, which extend the currently known family of 3D massless particles. These ‘‘Kane fermions’’ share many features with previously discussed Weyl and Dirac fermions: optical absorption which is linear in frequency, Landau levels and their Zeeman splitting, which are proportional to  $\sqrt{B}$  and rigidly related to each other. However, the relation between the spin and orbital splitting for massless Kane fermions is different from that for the ultra-relativistic Dirac electrons or Weyl fermions, which is one manifestation of their inequivalence. An important difference from massless electrons in Weyl semimetals is that the massless fermions in MCT are not protected by symmetry or topology; rather, we have engineered the conical dispersion by fine tuning a system parameter, cadmium concentration, which is extremely homogeneous over a macroscopic thickness. This lack of protection, in fact, may represent a major advantage for potential applications: the very robustness of semimetals protected by symmetry or topology makes them hard to manipulate (e.g., to introduce a small controllable gap), while the band structure of the MCT can be engineered at will, as our work shows. The high degree of technological control over this material opens further perspectives for its use in electronic devices, where one could benefit from the peculiar properties of massless fermions, such as the suppressed backscattering (Klein paradox) and the related inefficient Auger-type recombination.

While our paper was under review, we have learned about several recent preprints,<sup>38–40</sup> where related the issues are discussed.

## Methods

The sample was grown using standard molecular-beam epitaxy on a (013)-oriented semi-insulating GaAs substrate. The

growth sequence started with ZnTe and CdTe transition regions, followed by the MCT epilayer with gradually changing cadmium content  $x$  (see Supplementary Information). The prepared MCT layer contains a region with  $x \approx 0.17$  of thickness  $d \approx 3.2 \mu\text{m}$ .

The absorption coefficient of MCT was measured in the transmission configuration. A macroscopic area of the sample of about  $4 \text{ mm}^2$  was exposed to the radiation of a global or mercury lamp, which was analyzed by a Fourier transform spectrometer, and via light-pipe optics delivered to the sample placed either in a superconducting solenoid or resistive coil. At low fields, the correction for the remanent field of the solenoid has been made. The transmitted light was detected by a composite bolometer placed directly below the sample, kept at a temperature of 1.8 K. The sample transmission  $T_B$  at a given magnetic field  $B$ , was normalized by the substrate transmission,  $T_S$ , measured in the absence of MCT. The absorption coefficient  $\lambda_B$  was determined from the relation  $T_B/T_S = \exp(-\lambda_B d)$ . This relation neglects the dielectric mismatch between MCT and GaAs. A significant mismatch would result in additional reflection and would produce a constant vertical shift of the curve in Fig. 2, so the straight line would not pass through the origin. The fact that it does, shows that the dielectric mismatch is indeed negligible. This implies  $\epsilon_\infty \approx 6$ , when the realistic cut-off energy  $\Omega = 1.5 \text{ eV}$  is assumed<sup>37</sup>.

## Acknowledgements

The authors acknowledge helpful discussions with T. Brauner, R. Grill, M. Grynberg, A. A. Nersesyan, V. Novák, M. L. Sadowski, and W. Zawadzki. The work has been supported by ERC project MOMB and by EuroMagNET II under the EU Contract No. 228043.

## Author contributions

The experiment was proposed by M.O. and M.P., underlying theory was formulated by D.M.B. The sample growth was performed by N.N.M. and S.A.D. The sample was characterized by M.Z., F.T., W.K. and V.I.G. Magneto-optical experiments were performed by M.O., G.M., M.Z., P.N., C.F. and A.L.B. All coauthors discussed the data. M.O., M.P. and D.M.B. wrote the manuscript.

\* milan.orlita@lncmi.cnrs.fr

<sup>1</sup> Charlier, J.-C., Blase, X., and Roche, S. Electronic and transport properties of nanotubes. *Rev. Mod. Phys.* **79**, 677–732 (2007).

<sup>2</sup> Novoselov, K. S. *et al.* Two-dimensional gas of massless Dirac fermions in graphene. *Nature* **438**, 197 (2005).

<sup>3</sup> Zhang, Y. B., Tan, Y. W., Stormer, H. L., and Kim, P. Experimental observation of the quantum Hall effect and Berry’s phase in graphene. *Nature* **438**, 201 (2005).

<sup>4</sup> König, M. *et al.* Quantum spin Hall insulator state in HgTe quantum wells. *Science* **318**(5851), 766–770 (2007).

<sup>5</sup> Hasan, M. Z. and Kane, C. L. Colloquium: Topological insulators. *Rev. Mod. Phys.* **82**, 3045–3067 (2010).

<sup>6</sup> Young, S. M. *et al.* Dirac semimetal in three dimensions. *Phys. Rev. Lett.* **108**, 140405 (2012).

<sup>7</sup> Wan, X., Turner, A. M., Viswanath, A., and Savrasov, S.

Y. Topological semimetal and Fermi-arc surface states in the electronic structure of pyrochlore iridates. *Phys. Rev. B* **83**, 205101 (2011).

<sup>8</sup> Yang, K.-Y., Lu, Y.-M., and Ran, Y. Quantum Hall effects in a Weyl semimetal: Possible application in pyrochlore iridates. *Phys. Rev. B* **84**, 075129 (2011).

<sup>9</sup> Wang, Z. *et al.* Dirac semimetal and topological phase transitions in  $A_3\text{Bi}$  ( $A = \text{Na}, \text{K}, \text{Rb}$ ). *Phys. Rev. B* **85**, 195320 (2012).

<sup>10</sup> Steinberg, J. A. *et al.* Bulk Dirac points in distorted spinels. arXiv:1309.5967 (2013).

<sup>11</sup> Singh, B. *et al.* Topological electronic structure and Weyl semimetal in the  $\text{TlBiSe}_2$  class of semiconductors. *Phys. Rev. B* **86**, 115208 (2012).

<sup>12</sup> Xu, S.-Y. *et al.* Topological Phase Transition and Texture Inversion in a Tunable Topological Insulator. *Science* **332**,

- 560–564 (2011).
- <sup>13</sup> Sato, T. *et al.* Unexpected mass acquisition of Dirac fermions at the quantum phase transition of a topological insulator. *Nature Phys.* **7**, 840–844 (2011).
  - <sup>14</sup> Zawadzki, W. Electron transport phenomena in small-gap semiconductors. *Advances in Physics* **23**, 435–522 (1974).
  - <sup>15</sup> Harman, T. C. *et al.* Low Electron Effective Masses and Energy Gap in  $\text{Cd}_x\text{Hg}_{1-x}\text{Te}$ . *Phys. Rev. Lett.* **7**, 403 (1961).
  - <sup>16</sup> McCombe, B. D., Wagner, R., and Prinz, G. Infrared pulsed gas laser studies of combined resonance and cyclotron-phonon resonance in  $\text{Hg}_{1-x}\text{Cd}_x\text{Te}$ . *Solid State Communications* **8**, 1687 – 1691 (1970).
  - <sup>17</sup> Groves, S. H., Harman, T. C., and Pidgeon, C. R. Interband magnetoreflection of  $\text{Hg}_{1-x}\text{Cd}_x\text{Te}$ . *Solid State Communications* **9**, 451 - 455 (1971).
  - <sup>18</sup> Guldner, Y., Rigaux, C., Mycielski, A., and Couder, Y. Magneto-optical investigation of  $\text{Hg}_{1-x}\text{Cd}_x\text{Te}$  mixed crystals II. Semiconducting configuration and semimetal  $\rightarrow$  semiconductor transition. *physica status solidi (b)* **82**, 149–158 (1977).
  - <sup>19</sup> Weiler, M. H. In *Defects, (HgCd)Se, (HgCd)Te*, Willardson, R. K. and Beer, A. C., editors, volume 16 of *Semiconductors and Semimetals*, 119 – 191. Elsevier (1981).
  - <sup>20</sup> Bernevig, B. A., Hughes, T. L., and Zhang, S.-C. Quantum spin Hall effect and topological phase transition in HgTe quantum wells. *Science* **314**, 1757–1761 (2006).
  - <sup>21</sup> Kane, E. O. Band structure of indium antimonide. *Journal of Physics and Chemistry of Solids* **1**, 249 – 261 (1957).
  - <sup>22</sup> Novik, E. G. *et al.* Band structure of semimagnetic  $\text{Hg}_{1-y}\text{Mn}_y\text{Te}$  quantum wells. *Phys. Rev. B* **72**, 035321 (2005).
  - <sup>23</sup> Yu, P. Y. and Cardona, M. *Fundamentals of Semiconductors*. (Springer, Heidelberg, 1996).
  - <sup>24</sup> Eq. 4 is valid for the intrinsic material at zero temperature,  $T = 0$ . It has been noted recently [see Burkov, A. A. and Balents, L., Weyl Semimetal in a Topological Insulator Multilayer. *Phys. Rev. Lett.* **107**, 127205 (2012)] that in the intrinsic case (zero Fermi energy) the limits  $\omega \rightarrow 0$  and  $T \rightarrow 0$  do not commute. As discussed below, our sample is not fully intrinsic (some small residual population in the conduction band is present), so the limit  $\omega \rightarrow 0$  is regularized by this residual population.
  - <sup>25</sup> Katsnelson, M. I., Novoselov, K. S., and Geim, A. K. Chiral tunnelling and the Klein paradox in graphene. *Nature Phys.* **2**, 620–625 (2006).
  - <sup>26</sup> Young, A. F. and Kim, P. Quantum interference and Klein tunnelling in graphene heterojunctions. *Nature Phys.* **5**, 222–226 (2009).
  - <sup>27</sup> Kuzmenko, A. B. *et al.* Universal optical conductance of graphite. *Phys. Rev. Lett.* **100**, 117401 (2008).
  - <sup>28</sup> Nair, R. R. *et al.* Fine structure constant defines visual transparency of graphene. *Science* **320**, 1308 (2008).
  - <sup>29</sup> Yu, P. Y. and Cardona, M. *Fundamentals of Semiconductors*. Springer, Heidelberg (1999).
  - <sup>30</sup> Berestetskii, V. B., Lifshitz, E. M., and Pitaevskii, L. P. (Pergamon, Oxford, 1971).
  - <sup>31</sup> Ashby, P. E. C. and Carbotte, J. P. Magneto-optical conductivity of Weyl semimetals. *Phys. Rev. B* **87**, 245131 (2013).
  - <sup>32</sup> Zhu, Z. *et al.* Angle-resolved Landau spectrum of electrons and holes in bismuth. *Phys. Rev. B* **84**, 115137 (2011).
  - <sup>33</sup> Orlita, M. *et al.* Dirac Fermions at the  $H$  Point of Graphite: Magnetotransmission Studies *Phys. Rev. Lett.* **100**, 136403 (2008).
  - <sup>34</sup> Witowski, A. M. *et al.* Quasiclassical cyclotron resonance of Dirac fermions in highly doped graphene. *Phys. Rev. B* **82**, 165305 (2010).
  - <sup>35</sup> Crassee, I. *et al.* Giant Faraday rotation in single- and multilayer graphene. *Nature Phys.* **7**, 48–51 (2011).
  - <sup>36</sup> Orlita, M. *et al.* Classical to quantum crossover of the cyclotron resonance in graphene: a study of the strength of intraband absorption. *New J. of Phys.* **14**, 095008 (2012).
  - <sup>37</sup> Hass, K. C., Ehrenreich, H., and Velický, B. Electronic structure of  $\text{Hg}_{1-x}\text{Cd}_x\text{Te}$ . *Phys. Rev. B* **27**, 1088–1100 (1983).
  - <sup>38</sup> Neupane, M. *et al.* Observation of a topological 3D Dirac semimetal phase in high-mobility  $\text{Cd}_3\text{As}_2$ . arXiv:1309.7892 (2013).
  - <sup>39</sup> Borisenko, S. *et al.* Experimental Realization of a Three-Dimensional Dirac Semimetal. arXiv:1309.7978 (2013).
  - <sup>40</sup> Liu, Z. K. *et al.* Discovery of a Three-dimensional Topological Dirac Semimetal,  $\text{Na}_3\text{Bi}$ . arXiv:1310.0391 (2013).

## Supplementary Information for

### *3D massless Kane fermions observed in a zinc-blende crystal*

by M. Orlita, D. M. Basko, M. S. Zholudev, F. Teppe, W. Knap, V. I. Gavrilenko, N. N. Mikhailov, S. A. Dvoretiskii, P. Neugebauer, C. Faugeras, A.-L. Barra, G. Martinez, and M. Potemski

#### I. SAMPLE STRUCTURE

The studied sample was grown using the standard MBE technique on the (013)-oriented semi-insulating GaAs substrate. The growth sequence started with ZnTe and CdTe transition (buffer) regions, followed by the MCT epilayer with gradually changing cadmium content  $x$ . The profile of cadmium content is shown in Fig. 6. The prepared MCT layer contains a region with  $x \approx 0.17$  of thickness  $d \approx 3.2 \mu\text{m}$ . The cadmium profile has been controlled during growth using in situ single wavelength ellipsometry, see, e.g., Ref. S1.

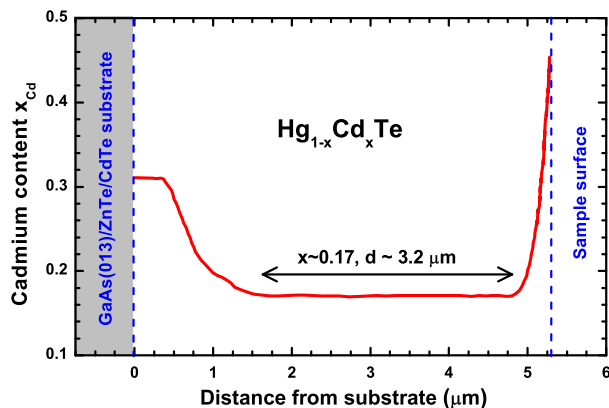


FIG. 6. The profile of cadmium content in the studied sample.

#### II. KANE MODEL AND THE EFFECTIVE BAND HAMILTONIAN

In zinc-blende semiconductors the orbital degeneracies of the conduction and valence bands are 1 and 3, respectively. At  $\mathbf{k} = 0$  we can choose a real Bloch function  $u_c(\mathbf{r})$  for the conduction band, and three real functions  $u_X(\mathbf{r})$ ,  $u_Y(\mathbf{r})$ ,  $u_Z(\mathbf{r})$  for the valence band. The function  $u_c(\mathbf{r})$  transforms according to the identical representation  $\Gamma_1$  of the crystal group  $T_d$ , while  $u_X(\mathbf{r})$ ,  $u_Y(\mathbf{r})$ ,  $u_Z(\mathbf{r})$  transform according to the vector  $\Gamma_{15}$  representation, equivalently to the functions  $x, y, z$ . Out of the three real functions  $u_\alpha(\mathbf{r})$  one can make linear combinations  $u_m(\mathbf{r})$  corresponding to eigenfunctions of the  $z$ -projection of the orbital angular momentum  $l = 1$ :

$$\begin{aligned}
 u_{+1} &= -\frac{i}{\sqrt{2}}(u_X + iu_Y), \\
 u_0 &= iu_Z, \\
 u_{-1} &= \frac{i}{\sqrt{2}}(u_X - iu_Y).
 \end{aligned}
 \tag{6}$$

The spin structure of the wave functions can be accounted for by introducing two spinors  $\chi_\uparrow, \chi_\downarrow$ , corresponding to the two values of the spin projection on the  $z$  axis. Spin-orbit interaction splits the  $2(2l+1)$ -fold degenerate valence band into two subspaces corresponding to the total angular momentum  $J = 1/2$  and  $J = 3/2$ , the latter manifold corresponding to the topmost valence band. Explicitly,

$$\begin{aligned}
 u_{3/2;+3/2} &= u_{+1}\chi_\uparrow, \\
 u_{3/2;+1/2} &= \sqrt{2/3}u_0\chi_\uparrow + \sqrt{1/3}u_{+1}\chi_\downarrow, \\
 u_{3/2;-1/2} &= \sqrt{2/3}u_0\chi_\downarrow + \sqrt{1/3}u_{-1}\chi_\uparrow, \\
 u_{3/2;-3/2} &= u_{-1}\chi_\downarrow, \\
 u_{1/2;+1/2} &= \sqrt{1/3}u_0\chi_\uparrow - \sqrt{2/3}u_{+1}\chi_\downarrow, \\
 u_{1/2;-1/2} &= -\sqrt{1/3}u_0\chi_\downarrow + \sqrt{2/3}u_{-1}\chi_\uparrow,
 \end{aligned}
 \tag{7}$$



It is convenient to arrange the basis vectors as

$$\begin{pmatrix} u_c\chi_\uparrow & u_{3/2,+3/2} & u_{3/2,-1/2} & u_{1/2,+1/2} & u_c\chi_\downarrow & u_{3/2,-3/2} & u_{3/2,+1/2} & u_{1/2,-1/2} \end{pmatrix} \quad (8)$$

$$= \begin{pmatrix} u_c\chi_\uparrow & u_X\chi_\uparrow & u_Y\chi_\uparrow & u_Z\chi_\uparrow & u_c\chi_\downarrow & u_X\chi_\downarrow & u_Y\chi_\downarrow & u_Z\chi_\downarrow \end{pmatrix} U, \quad (9)$$

$$U = \begin{pmatrix} 1 & 0 & 0 & 0 & 0 & 0 & 0 & 0 \\ 0 & -\sqrt{1/2}i & \sqrt{1/6}i & 0 & 0 & 0 & 0 & \sqrt{1/3}i \\ 0 & \sqrt{1/2} & \sqrt{1/6} & 0 & 0 & 0 & 0 & \sqrt{1/3} \\ 0 & 0 & 0 & \sqrt{1/3}i & 0 & 0 & \sqrt{2/3}i & 0 \\ 0 & 0 & 0 & 0 & 1 & 0 & 0 & 0 \\ 0 & 0 & 0 & \sqrt{1/3}i & 0 & \sqrt{1/2}i & -\sqrt{1/6}i & 0 \\ 0 & 0 & 0 & -\sqrt{1/3} & 0 & \sqrt{1/2} & \sqrt{1/6} & 0 \\ 0 & 0 & \sqrt{2/3}i & 0 & 0 & 0 & 0 & -\sqrt{1/3}i \end{pmatrix}, \quad (10)$$

then the time reversal matrix is just  $\sigma_y$ , the second Pauli matrix acting in the  $2 \times 2$  space made of  $4 \times 4$  blocks.

In this basis, the electronic Hamiltonian at  $\mathbf{k} = 0$  is given by

$$H(\mathbf{k} = 0) = \begin{pmatrix} E_g & 0 & 0 & 0 & 0 & 0 & 0 & 0 \\ 0 & 0 & 0 & 0 & 0 & 0 & 0 & 0 \\ 0 & 0 & 0 & 0 & 0 & 0 & 0 & 0 \\ 0 & 0 & 0 & -\Delta & 0 & 0 & 0 & 0 \\ 0 & 0 & 0 & 0 & E_g & 0 & 0 & 0 \\ 0 & 0 & 0 & 0 & 0 & 0 & 0 & 0 \\ 0 & 0 & 0 & 0 & 0 & 0 & 0 & 0 \\ 0 & 0 & 0 & 0 & 0 & 0 & 0 & -\Delta \end{pmatrix}, \quad (11)$$

where the energy is counted from the top of the  $J = 3/2$  valence band.  $\Delta$  is the spin-orbit splitting between the  $J = 3/2$  and the  $J = 1/2$  valence bands. The band gap is parametrized by  $E_g \approx (x - x_c) \cdot 1.9$  eV, see Ref. S2. Since  $E_g < 0$  at  $x < x_c$ , the semimetallic MCT is sometimes called a negative-gap semiconductor.

The linear in  $\mathbf{k}$  terms in the effective band Hamiltonian are obtained in the first order of the  $\mathbf{k} \cdot \mathbf{p}$  perturbation theory. The momentum matrix elements between the conduction and the valence band Bloch functions are determined by

$$\int u_\alpha(\mathbf{r}) \frac{\partial u_c(\mathbf{r})}{\partial x_\beta} d^3\mathbf{r} = P\delta_{\alpha\beta}, \quad (12)$$

where  $P$  is the Kane's matrix element, and  $2P^2/m_0 \equiv E_P$  is called Kane's energy ( $m_0$  is the free electron mass).

The effective Hamiltonian to  $O(k)$  is given by:

$$H(\mathbf{k}) = H(\mathbf{k} = 0) + U^\dagger \left[ \frac{P}{m_0} \begin{pmatrix} 0 & ik_x & ik_y & ik_z \\ -ik_x & 0 & 0 & 0 \\ -ik_y & 0 & 0 & 0 \\ -ik_z & 0 & 0 & 0 \end{pmatrix} \otimes \begin{pmatrix} 1 & 0 \\ 0 & 1 \end{pmatrix} \right] U = \begin{pmatrix} E_g & vk_+\sqrt{3}/2 & -vk_-/2 & -vk_z/\sqrt{2} & 0 & 0 & -vk_z & -vk_-/\sqrt{2} \\ vk_-\sqrt{3}/2 & 0 & 0 & 0 & 0 & 0 & 0 & 0 \\ -vk_+/2 & 0 & 0 & 0 & -vk_z & 0 & 0 & 0 \\ -vk_z/\sqrt{2} & 0 & 0 & -\Delta & -vk_-/\sqrt{2} & 0 & 0 & 0 \\ 0 & 0 & -vk_z & -vk_+/\sqrt{2} & E_g & -vk_-\sqrt{3}/2 & vk_+/2 & vk_z/\sqrt{2} \\ 0 & 0 & 0 & 0 & -vk_+\sqrt{3}/2 & 0 & 0 & 0 \\ -vk_z & 0 & 0 & 0 & vk_-/2 & 0 & 0 & 0 \\ -vk_+/\sqrt{2} & 0 & 0 & 0 & vk_z/\sqrt{2} & 0 & 0 & -\Delta \end{pmatrix}, \quad (13)$$

where  $v \equiv \sqrt{3/2}P/m_0$ , and  $k_\pm \equiv k_x \pm ik_y$ . This Hamiltonian obeys the time-reversal symmetry,  $\sigma_y H^*(\mathbf{k})\sigma_y = H(-\mathbf{k})$ , where  $\sigma_y$  is the second Pauli matrix acting in the  $2 \times 2$  space made of  $4 \times 4$  blocks. The eigenvalues of the Hamiltonian (13) can be found from the equation

$$\det(H - E) = E^2 \{ E^3 + (\Delta - E_g)E^2 - [E_g\Delta + (3/2)v^2k^2]E - v^2k^2\Delta \}^2 = 0. \quad (14)$$

They do not depend on the direction of  $\mathbf{k}$ .

In the limit of large  $\Delta$ , the Hamiltonian can be easily projected on the subspace, orthogonal to the the split-off band. If we are not interested in terms quadratic in  $\mathbf{k}$ , the projection is done by simply eliminating the fourth and the eight row and column of the matrix in Eq. (13):

$$H(\mathbf{k}) = \begin{pmatrix} E_g & vk_+\sqrt{3}/2 & -vk_-/2 & 0 & 0 & -vk_z \\ vk_-\sqrt{3}/2 & 0 & 0 & 0 & 0 & 0 \\ -vk_+/2 & 0 & 0 & -vk_z & 0 & 0 \\ 0 & 0 & -vk_z & E_g & -vk_-\sqrt{3}/2 & vk_+/2 \\ 0 & 0 & 0 & -vk_+\sqrt{3}/2 & 0 & 0 \\ -vk_z & 0 & 0 & vk_-/2 & 0 & 0 \end{pmatrix}. \quad (15)$$

This matrix has three doubly-degenerate eigenvalues:

$$E_{\mathbf{k}} = 0, \quad E_{\mathbf{k}} = \frac{E_g}{2} \pm \sqrt{\frac{E_g^2}{4} + v^2 k^2}. \quad (16)$$

The eigenvalue  $E = 0$  corresponds to the heavy-hole band, which in this approximation is completely flat.

Let us see how the existence of the flat band follows from the property  $U_c H(\mathbf{k}) U_c = -H(\mathbf{k})$ , with  $H(\mathbf{k})$  given by Eq. (15) and  $U_c = \text{diag}(1, -1, -1, 1, -1, -1)$ . Consider the general situation: an  $(n+m) \times (n+m)$  matrix  $A$ , anticommute with a matrix  $U_c$  which has  $m$  eigenvalues equal to 1, and  $n$  eigenvalues equal to  $-1$ , and  $m < n$ . Let us work in the basis of the eigenvectors of  $U_c$ , which are arranged in such an order that  $U_c = \text{diag}(-1, \dots, -1, 1, \dots, 1)$ . The condition  $U_c A U_c = -A$  implies that in this basis the matrix  $A$  has the following block structure:

$$A = \begin{pmatrix} 0_{n \times n} & A'_{n \times m} \\ A''_{m \times n} & 0_{m \times m} \end{pmatrix}. \quad (17)$$

Consider now the  $n$ -dimensional subspace of column vectors  $\underline{x} = (x_1, x_2, \dots, x_n, 0, \dots, 0)^T$ . All these vectors satisfy the first  $n$  equations of the linear system  $A \underline{x} = 0$ . The remaining  $m$  equations leave an  $(n-m)$  dimensional subspace of solutions  $A \underline{x} = 0$ , which corresponds to the zero eigenvalue of  $A$  with multiplicity  $n-m$ .

### III. OPTICAL ABSORPTION AT ZERO MAGNETIC FIELD

Let us start from the standard expression for the optical conductivity, obtained from the Kubo formula for the response of the current to the monochromatically oscillating vector potential:

$$\sigma_{ij}(\omega) = -ie^2 \int \frac{d^3 \mathbf{k}}{(2\pi)^3} \sum_{l, l'=1}^6 \frac{f_{l, \mathbf{k}} - f_{l', \mathbf{k}}}{E_{l, \mathbf{k}} - E_{l', \mathbf{k}}} \frac{\langle l, \mathbf{k} | v_i | l', \mathbf{k} \rangle \langle l', \mathbf{k} | v_j | l, \mathbf{k} \rangle}{\omega - E_{l', \mathbf{k}} + E_{l, \mathbf{k}} + i0^+}. \quad (18)$$

Here  $l, l' = 1, \dots, 6$  label the eigenstates of  $H(\mathbf{k})$  which is given by Eq. (15),  $f_{l, \mathbf{k}}$  are the occupations of these eigenstates, and the velocity matrices are  $v_i = \partial H(\mathbf{k}) / \partial k_i = v J_i$ , where  $i, j = x, y, z$  label the Cartesian components.

To calculate the velocity matrix elements, we note that the projection of the vector  $\mathbf{J}$  on an arbitrary direction  $\mathbf{n} = (\sin \vartheta \cos \varphi, \sin \vartheta \sin \varphi, \cos \vartheta)$ , determined by the spherical angles  $\vartheta, \varphi$ , can be related to  $J_z$  by a rotation

$$\mathbf{J} \cdot \mathbf{n} = J_x \sin \vartheta \cos \varphi + J_y \sin \vartheta \sin \varphi + J_z \cos \vartheta = U_\varphi^\dagger (J_x \sin \vartheta + J_z \cos \vartheta) U_\varphi = U_\varphi^\dagger U_\vartheta^\dagger J_z U_\vartheta U_\varphi, \quad (19)$$

$$U_\varphi = \text{diag} \left( e^{i\varphi/2}, e^{3i\varphi/2}, e^{-i\varphi/2}, e^{-i\varphi/2}, e^{-3i\varphi/2}, e^{i\varphi/2} \right), \quad (20)$$

$$U_\vartheta = \begin{pmatrix} c & 0 & 0 & s & 0 & 0 \\ 0 & c^3 & \sqrt{3}cs^2 & 0 & s^3 & \sqrt{3}c^2s \\ 0 & \sqrt{3}cs^2 & c^3 - 2cs^2 & 0 & \sqrt{3}c^2s & s^3 - 2c^2s \\ -s & 0 & 0 & c & 0 & 0 \\ 0 & -s^3 & -\sqrt{3}c^2s & 0 & c^3 & \sqrt{3}cs^2 \\ 0 & -\sqrt{3}c^2s & -s^3 + 2c^2s & 0 & \sqrt{3}cs^2 & c^3 - 2cs^2 \end{pmatrix}, \quad c \equiv \cos \frac{\vartheta}{2}, \quad s \equiv \sin \frac{\vartheta}{2}. \quad (21)$$

Thus, the eigenstates  $|l, \mathbf{k}\rangle$  for an arbitrary direction of  $\mathbf{k}$  can be related to those for  $\mathbf{k}$  along  $z$  by  $|l, \mathbf{k}\rangle = U_\varphi^\dagger U_\vartheta^\dagger |l, k, z\rangle$ , where  $\vartheta, \varphi$  are the spherical angles of  $\mathbf{k}$ .

By symmetry, the tensor structure of the conductivity is trivial,  $\sigma_{ij}(\omega) = \sigma(\omega)$ . This can also be shown by the direct calculation, whose details we do not give, but which is fully analogous to the one given below. We calculate just one component,  $\sigma_{zz}$ . Since the energies  $E_{l, \mathbf{k}}$  depend only on  $|\mathbf{k}|$ , we can integrate over the angles using Eq. (19):

$$\mathcal{J}_{ll'} = \int \sin \vartheta d\vartheta d\varphi |\langle l, \mathbf{k} | J_z | l', \mathbf{k} \rangle|^2 = \frac{8\pi}{3} |\langle l, k, z | J_x | l', k, z \rangle|^2 + \frac{4\pi}{3} |\langle l, k, z | J_z | l', k, z \rangle|^2. \quad (22)$$

The eigenvectors of the Hamiltonian (15) for  $\mathbf{k}$  along the  $z$  axis are (in the order of decreasing energy)

$$\begin{pmatrix} S \\ 0 \\ 0 \\ 0 \\ 0 \\ -C \end{pmatrix}, \begin{pmatrix} 0 \\ 0 \\ S \\ -C \\ 0 \\ 0 \end{pmatrix}, \begin{pmatrix} 0 \\ 1 \\ 0 \\ 0 \\ 0 \\ 0 \end{pmatrix}, \begin{pmatrix} 0 \\ 0 \\ 0 \\ 0 \\ 1 \\ 0 \end{pmatrix}, \begin{pmatrix} C \\ 0 \\ 0 \\ 0 \\ 0 \\ S \end{pmatrix}, \begin{pmatrix} 0 \\ 0 \\ 0 \\ 0 \\ 0 \\ 0 \end{pmatrix},$$

where we have denoted

$$C = \cos \left( \frac{\phi_g}{2} + \frac{\pi}{4} \right), \quad S = \sin \left( \frac{\phi_g}{2} + \frac{\pi}{4} \right), \quad \phi_g \equiv \arcsin \frac{E_g/2}{\sqrt{E_g^2/4 + v^2 k^2}}.$$

This gives

$$\mathcal{J}_{U'} = \frac{\pi}{3} \begin{pmatrix} 4c_g^2 & 2s_g^2 & 3(1+s_g) & 0 & 4s_g^2 & 2c_g^2 \\ 2s_g^2 & 4c_g^2 & 0 & 3(1-s_g) & 2c_g^2 & 4s_g^2 \\ 3(1+s_g) & 0 & 0 & 0 & 3(1-s_g) & 0 \\ 0 & 3(1-s_g) & 0 & 0 & 0 & 3(1+s_g) \\ 4s_g^2 & 2c_g^2 & 3(1-s_g) & 0 & 4c_g^2 & 2s_g^2 \\ 2c_g^2 & 4s_g^2 & 0 & 3(1+s_g) & 2s_g^2 & 4c_g^2 \end{pmatrix}, \quad c_g = \cos \phi_g, \quad s_g = \sin \phi_g. \quad (23)$$

Substituting this into Eq. (18), we finally obtain

$$\begin{aligned} \text{Re } \sigma(\omega > 0) &= \frac{\pi^2}{3} \frac{e^2}{v\omega} \int_0^\infty \frac{\xi^2 d\xi}{8\pi^3} \left[ 6\delta\left(\frac{E_g}{2} + \sqrt{\frac{E_g^2}{4} + \xi^2} - \omega\right) + 4\left(1 + \frac{E_g^2}{E_g^2 + 4\xi^2}\right) \delta\left(\sqrt{E_g^2 + 4\xi^2} - \omega\right) \right] = \\ &= \frac{e^2}{4\pi v} \left[ \theta(2\omega - |E_g| - E_g) \left(1 - \frac{E_g}{2\omega}\right) \sqrt{\omega^2 - \omega E_g} + \frac{1}{16} \theta(\omega - |E_g|) \left(1 + \frac{E_g}{\omega^2}\right) \sqrt{\omega^2 - E_g^2} \right]. \end{aligned} \quad (24)$$

For the gapless case,  $E_g = -$ , we obtain  $\text{Re } \sigma(\omega > 0) = \frac{13}{12} \omega \frac{e^2}{v\pi}$ . The imaginary part of the dielectric function,  $\varepsilon(\omega) = 1 + i\sigma(\omega)/(\varepsilon_0\omega)$ , then becomes  $\text{Im } \varepsilon(\omega > 0) = \frac{13}{12} \frac{e}{v} \alpha$ , where  $\alpha$  is the fine structure constant.

#### IV. LANDAU LEVELS

In the presence of a magnetic field, described by the vector potential in the Landau gauge  $A_x = -By$ ,  $A_y = A_z = 0$ , we make the standard Peierls substitution  $\mathbf{p} \rightarrow \mathbf{p} - e\mathbf{A}$  in the Hamiltonian (15), and seek the eigenstates in the form

$$\psi(x, y) = e^{ip_x x} \begin{pmatrix} x_\uparrow \Phi_{n-1} & y_\uparrow \Phi_n & z_\uparrow \Phi_{n-2} & x_\downarrow \Phi_{n-2} & y_\downarrow \Phi_{n-3} & z_\downarrow \Phi_{n-1} \end{pmatrix}^T, \quad (25)$$

where  $\Phi_n = \Phi_n(y + p_x l_B^2)$  are the harmonic oscillator wave functions and  $l_B$  is the magnetic length. It can be checked directly that the form (25) is preserved upon action on  $\psi(x, y)$  by the Hamiltonian. The coefficients satisfy the following linear system (we denote  $\zeta \equiv p_z l_B$  for brevity):

$$\begin{aligned} \frac{E_g - E}{v/l_B} x_\uparrow + \sqrt{\frac{3n}{2}} y_\uparrow - \sqrt{\frac{n-1}{2}} z_\uparrow - \zeta z_\downarrow &= 0, \\ \sqrt{\frac{3n}{2}} x_\uparrow - \frac{E}{v/l_B} y_\uparrow &= 0, \\ -\sqrt{\frac{n-1}{2}} x_\uparrow - \frac{E}{v/l_B} z_\uparrow - \zeta x_\downarrow &= 0, \\ -\zeta z_\uparrow + \frac{E_g - E}{v/l_B} x_\downarrow - \sqrt{\frac{3(n-2)}{2}} y_\downarrow + \sqrt{\frac{n-1}{2}} z_\downarrow &= 0, \\ -\sqrt{\frac{3(n-2)}{2}} x_\downarrow - \frac{E}{v/l_B} y_\downarrow &= 0, \\ -\zeta x_\uparrow + \sqrt{\frac{n-1}{2}} x_\downarrow - \frac{E}{v/l_B} z_\downarrow &= 0. \end{aligned} \quad (26)$$

Its analysis is especially simple at  $p_z = 0$ , when the system is split into two decoupled  $3 \times 3$  blocks for  $x_\uparrow, y_\uparrow, z_\uparrow$  and  $x_\downarrow, y_\downarrow, z_\downarrow$ , respectively. It is convenient to shift  $n-1 \rightarrow n$  in the “ $\downarrow$ ” block. In each block, the Landau levels can be labeled by  $n = 0, 1, 2, \dots$ ,  $\zeta = -1, 0, 1$ . At  $n = 1$ , only  $\zeta = \pm 1$  are allowed, while at  $n = 0$  only  $\zeta = 0$  exists:

$$E_{n,\zeta,\uparrow\downarrow} = \zeta^2 \frac{E_g}{2} + \zeta \sqrt{\frac{E_g^2}{4} + \frac{v^2}{2l_B^2} (4n - 2 \pm 1)}, \quad (27)$$

$$\psi_{n>1,0,\uparrow} = \frac{1}{\sqrt{4n-1}} \begin{pmatrix} 0 \\ \sqrt{n-1} \Phi_n \\ \sqrt{3n} \Phi_{n-2} \end{pmatrix}, \quad \psi_{0,0,\uparrow} = \begin{pmatrix} 0 \\ \phi_0 \\ 0 \end{pmatrix}, \quad (28)$$

$$\psi_{n>0,\pm 1,\uparrow} = \frac{1}{\sqrt{E^2 + (2n-1/2)(v/l_B)^2}} \begin{pmatrix} -E \Phi_{n-1} \\ -\sqrt{3n/2} (v/l_B) \Phi_n \\ \sqrt{(n-1)/2} (v/l_B) \Phi_{n-2} \end{pmatrix}, \quad (29)$$

$$\psi_{n>1,0,\downarrow} = \frac{1}{\sqrt{4n-3}} \begin{pmatrix} 0 \\ \sqrt{n} \Phi_{n-2} \\ \sqrt{3(n-1)} \Phi_n \end{pmatrix}, \quad \psi_{0,0,\downarrow} = \begin{pmatrix} 0 \\ 0 \\ \Phi_0 \end{pmatrix}, \quad (30)$$

$$\psi_{n>0,\pm 1,\downarrow} = \frac{1}{\sqrt{E^2 + (2n-3/2)(v/l_B)^2}} \begin{pmatrix} -E \Phi_{n-1} \\ \sqrt{3(n-1)/2} (v/l_B) \Phi_{n-2} \\ -\sqrt{n/2} (v/l_B) \Phi_n \end{pmatrix}. \quad (31)$$

The selection rules for the optical absorption at  $p_z = 0$  are obtained by calculating the matrix elements of  $J_{\pm} = J_x \pm iJ_y$ :

$$\langle n' \zeta' \sigma' | J_{\pm} | n \zeta \sigma \rangle \propto \delta_{\sigma \sigma'} \delta_{n', n-1} (1 - \delta_{\zeta 0} \delta_{\zeta' 0}). \quad (32)$$

At  $p_z \neq 0$ , the Landau levels can be found directly from the system (26):

$$E_{n, \zeta, \uparrow \downarrow} = \zeta^2 \frac{E_g}{2} + \zeta \sqrt{\frac{E_g^2}{4} + \frac{v^2}{2l_B^2} (4n - 2 \pm 1) + v^2 p_z^2}. \quad (33)$$

For  $E_g = 0$  this expression reduces to Eq. (5) of the main text.

### References:

[S1] N. N. Mikhailov, R. N. Smirnov, S. A. Dvoretzky, Yu. G. Sidorov, V. A. Shvets, E. V. Spesivtsev and S. V. Rykhlitski, *Int. J. Nanotechnology* **3**, 120 (2006).

[S2] M. H. Weiler, in *Semiconductors and Semimetals, vol. 16* ed. by R. K. Willardson and A. C. Beer (Elsevier, 1981).

---